Extended volumetric scheme for lattice Boltzmann models

Hongli Fan, Raoyang Zhang, and Hudong Chen

Exa Corporation, 3 Burlington Woods Drive, Burlington, Massachusetts, 01803, USA

An extended volumetric scheme is proposed for lattice Boltzmann (LB) models. This scheme is particularly desirable for multispeed LB models due to its removal of nonlocal advection. It recovers the same macroscopic hydrodynamics as the standard lattice Boltzmann method without any further treatments. This scheme achieves an effectively reduced Courant-Friedrichs-Lewy number so that numerical stability is significantly enhanced for high Reynolds number simulations while maintaining the same order of numerical accuracy.

PACS number(s): 02.70.−c, 47.11.−j

I. INTRODUCTION

The lattice Boltzmann method (LBM) is a viable computational fluid dynamics (CFD) tool for simulating complex fluid flows [1–4]. It has many attractive advantages over conventional CFD methods, such as intrinsic parallelism, simplicity of coding, capability of handling complex geometries, and ease of incorporating multiphase interactions, to name a few. Nevertheless, the standard LBM often suffers from numerical instability when viscosity is greatly reduced. This is partially due to the fact that LBM marginally satisfies the Courant-Friedrichs-Lewy (CFL) condition [5,6]. Such an undesirable feature limits LBM applications for simulation of flows at high Reynolds number, unless higher grid resolutions are used. Motivated in part by such a consideration, several volumetric schemes have been introduced previously [7,8]. The essential concept of a volumetric scheme is to reduce effectively the CFL number by reducing the particle propagation time step to achieve better numerical stability while maintaining the same numerical accuracy. Though details are different, all these schemes demonstrate a better stability than the standard LBM. In this paper, we present a further extension of a volumetric scheme from the work of Ref. [8]. This scheme is specially suitable for LBM models involving multiple speeds greater than unity.

The standard multispeed LBM with the popular Bhatnagar-Gross-Krook (BGK) collision operator [9] can be represented by the following evolution equation for particle distribution function, $f_{ij}(\mathbf{x},t)$,

$$f_{ij}(\mathbf{x}+\mathbf{c}_{ij}\Delta t, t+\Delta t) = f'_{ij}(\mathbf{x},t),$$

$$f'_{ij}(\mathbf{x},t) = f_{ij}(\mathbf{x},t) + \Omega_{ij}(\mathbf{x},t),$$

$$\Omega_{ij}(\mathbf{x},t) = -\frac{f_{ij}(\mathbf{x},t) - f^{eq}_{ij}(\mathbf{x},t)}{\tau}, \quad (i=1,\ldots,b_j; j=1,\ldots,J),$$

(1)

where $\mathbf{c}_{ij}$ is the discrete particle velocity and τ is a relaxation time to local equilibrium. Δt is the lattice time increment, and conventionally $\Delta t = 1$ for convenience. b_j denotes the total number of particle velocity directions for a given energy level ϵ_j $(\equiv |\mathbf{c}_{ij}|^2/2)$, and J represents the total number of energy levels. The above dynamics consists of two alternating operations: advection and collision. During each time

increment, $f_{ij}(\mathbf{x},t)$ advects to the neighbor cell at location $\mathbf{x}+\mathbf{c}_{ij}$ according to velocity $\mathbf{c}_{ij}$, and then it collides with distribution functions of other particle velocities in the same lattice cell. The collision term Ω_{ij} is constrained to satisfy the local conservations of mass, momentum and energy. $f'_{ij}(\mathbf{x},t)$ represents the particle distribution after a collision, i.e., the postcollide distribution. With the appropriately prescribed local equilibrium distribution function $f^{eq}_{ij}(\mathbf{x},t)$, the macroscopic dynamics of the Navier-Stokes equations is recovered in LBM at the long wavelength and low frequency limit. The hydrodynamics quantities of the fluid flow, such as fluid density ρ, velocity $\mathbf{u}$ and energy e, are determined by taking moments of distribution function $f_{ij}(\mathbf{x},t)$,

$$\rho(\mathbf{x},t) = \sum_{ij} f_{ij}(\mathbf{x},t),$$

(2)

$$\rho(\mathbf{x},t)\mathbf{u}(\mathbf{x},t) = \sum_{ij} \mathbf{c}_{ij} f_{ij}(\mathbf{x},t),$$

(3)

$$\rho(\mathbf{x},t)e(\mathbf{x},t) = \rho(\mathbf{x},t)\left[\frac{D}{2}T(\mathbf{x},t) + \frac{1}{2}\mathbf{u}^2(\mathbf{x},t)\right] = \sum_{ij} \epsilon_j f_{ij}(\mathbf{x},t),$$

(4)

where $T(\mathbf{x},t)$ is temperature, and D refers to dimension of the lattice of a given lattice Boltzmann (LB) model.

The original concept and general formulation of volumetric LB model was described by Chen in 1998 [7]. The scheme obeys exact conservation laws for arbitrary mesh structures and resolutions. The volumetric-based fractional particle advection is weighted by the overlapping area of the moving cell and its neighboring cells. As a result, this scheme is relatively complicated and is not very efficient computationally. The scheme of Zhang *et al.* [8] is a direct extension of Chen's original model but with significant simplifications in particle advection. It only advects a fraction of particles from their original site $\mathbf{x}$ to the unique destination site $\mathbf{x}+\mathbf{c}_{ij}$ indicated by particle velocity $\mathbf{c}_{ij}$. Besides algorithmic simplicity, the advection process is exactly along the particle microscopic velocity characteristic lines, so that numerical diffusion is minimized. However, for LB models involving multiple speeds greater than unity, scheme of Zhang *et al.* requires more than one lattice spacing distance in each advection step. This nonlocal advection is not desirable from

parallel computation point of view, especially for applications involving complex geometries. To remove such a nonlocality while still maintaining the other advantages, we present in this paper a further extended volumetric scheme to Zhang *et al.* together with some numerical verifications.

II. DESCRIPTION OF THE EXTENDED VOLUMETRIC SCHEME

For a typical LB model possessing multiple speed levels N (>1), the particle speed level can be represented in such a way that for any particle at speed level k ($k=1,2,\ldots,N-1$), the Cartesian component of its velocity is either zero or $\pm k$ single integer value. Thus, the lattice velocity can be expressed as

$$\mathbf{c}_{ik} = k\hat{c}_{ik},$$

where $\hat{c}_{ik}$ now only has components of either 0 or ± 1. Obviously, lattice site $\mathbf{x}+\hat{c}_{ik}$ is a nearest neighbor site of $\mathbf{x}$ along the direction $\mathbf{c}_{ik}$. Note here that the speed-level k may not be identical to the energy level j subscribed in the Eq. (1).

The basic idea of the present volumetric scheme is to realize a particle advection process for all speed levels that only involves nearest neighbor sites per time step. To achieve this local advection, instead of an overall factor of p [8], the fractional advection factor is defined per speed level k, namely

$$p_k = kp.$$

With the above definition, we divide the particle distribution $f'_{ik}(\mathbf{x},t)$ into two parts, $f^{move}_{ik}(\mathbf{x},t)$ and $f^{nonmove}_{ik}(\mathbf{x},t)$:

$$f^{move}_{ik}(\mathbf{x},t) = p_k[f'_{ik}(\mathbf{x},t) + \delta f^{move}_{ik}(\mathbf{x},t)], \tag{5}$$

$$f^{nonmove}_{ik}(\mathbf{x},t) = (1-p_k)[f'_{ik}(\mathbf{x},t) + \delta f^{nonmove}_{ik}(\mathbf{x},t)], \tag{6}$$

where

$$\delta f^{move}_{ik}(\mathbf{x},t) = \frac{(1-p_k)}{2}\delta f'_{ik}(\mathbf{x},t), \tag{7}$$

$$\delta f^{nonmove}_{ik}(\mathbf{x},t) = -\frac{p_k}{2}\delta f'_{ik}(\mathbf{x},t), \tag{8}$$

and

$$\delta f'_{ik}(\mathbf{x},t) = f'_{ik}(\mathbf{x}+\hat{c}_{ik},t) - f'_{ik}(\mathbf{x},t). \tag{9}$$

From the above, one can see that the mass conservation is strictly enforced by $f^{move}_{ik}+f^{nonmove}_{ik}=f'_{ik}$. The term $\delta f'_{ik}$ arises from the use of a first-order ("downwind") approximation to the local particle distribution gradient in a volumetric representation. This ensures that the overall accuracy of the extended volumetric scheme is second order [7].

The present extended volumetric advection process can be written as

$$f_{ik}(\mathbf{x},t+1) = f^{move}_{ik}(\mathbf{x}-\hat{c}_{ik},t) + f^{nonmove}_{ik}(\mathbf{x},t). \tag{10}$$

That is, the moving part in cell $\mathbf{x}$ is advected to the nearest neighbor cell $\mathbf{x}+\hat{c}_{ik}$, while the nonmove part stays in $\mathbf{x}$. The

postadvect distribution is a result of the summation of the two parts after the advection step. As the consequence of such an advection, we obtain the LB equation for our scheme as

$$f_{ik}(\mathbf{x},t+1) = p_k\left[f'_{ik}(\mathbf{x}-\hat{c}_{ik},t) + \frac{(1-p_k)}{2}\delta f'_{ik}(\mathbf{x}-\hat{c}_{ik},t)\right]$$
$$+ (1-p_k)\left[f'_{ik}(\mathbf{x},t) - \frac{p_k}{2}\delta f'_{ik}(\mathbf{x},t)\right]. \tag{11}$$

In order to ensure a valid nearest neighbor advection ($0 < p_k \leq 1$), the overall fraction factor p must be bounded as $0 < p \leq 1/(N-1)$ for an N-speed LB model. Other than the nearest neighbor only advection, the present scheme is very similar in form to that of Zhang *et al.* [8]. Indeed, for LB models only involve "speed-1" particle distributions, the two schemes become identical.

With the Taylor expansion of Eq. (11) and the use of Eq. (9), it is easily shown that the postadvect distribution, $f_{ik}(\mathbf{x},t+1)=f'_{ik}(\mathbf{x}-p\mathbf{c}_{ik},t)$, is satisfied up to the second order in spatial derivative. This is the same as the standard LBM with the understanding that each physical time step in this scheme is only p fraction of a time step in the standard LBM, which is to be further verified as bellows.

It is relatively straightforward to derive the resulting hydrodynamic equations from this LB scheme. A standard Chapman Enskog expansion [10] is employed here

$$\frac{\partial}{\partial t} = \varepsilon\frac{\partial}{\partial t_1} + \varepsilon^2\frac{\partial}{\partial t_2}, \quad \mathbf{\nabla} = \varepsilon\mathbf{\nabla}_1 \tag{12}$$

and

$$f_{ij} = f^{eq}_{ij} + \varepsilon f^{(1)}_{ij} + \varepsilon^2 f^{(2)}_{ij} + O(\varepsilon^3), \tag{13}$$

where ε is a small perturbation value representing the ratio of lattice scales to macroscopic hydrodynamic scales. Applying the above expansion together with the Taylor expanded form of Eq. (11) up to second order, we obtain a set of differential equations below

$$\frac{\partial f^{eq}_{ij}}{\partial t_1} + p\mathbf{c}_{ij}\cdot\mathbf{\nabla}_1 f^{eq}_{ij} = -\frac{f^{(1)}_{ij}}{\tau}, \tag{14}$$

at order ε, and

$$\frac{\partial f^{eq}_{ij}}{\partial t_2} + \left(1-\frac{1}{2\tau}\right)\left(\frac{\partial f^{(1)}_{ij}}{\partial t_1} + p\mathbf{c}_{ij}\cdot\mathbf{\nabla}_1 f^{(1)}_{ij}\right) = -\frac{f^{(2)}_{ij}}{\tau} \tag{15}$$

at order ε^2. The above analysis has used the relationship $p_j\hat{c}_{ij}=p\mathbf{c}_{ij}$. Since the factor p is an overall constant, the energy level subscript j can be treated as representing the speed level for convenience. Compared with the equations derived from standard LBM [3,8], the only difference in the above forms is that $\mathbf{c}_{ij}$ is replaced by $p\mathbf{c}_{ij}$. It is straightforward to see that this is effectively achieving a reduced time step size p (≤ 1), instead of unity in the standard LBM. Hence, a particle only advects a distance of $p\mathbf{c}_{ij}$ per each time step. After taking moment summations over $\mathbf{c}_{ij}$ to Eq. (14) and (15), we obtain the hydrodynamic equations
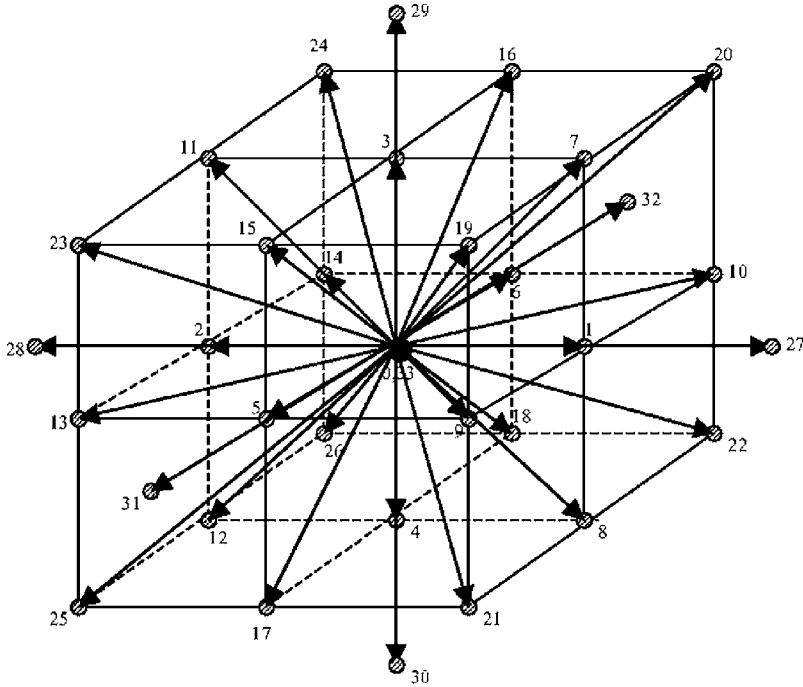
FIG. 1. Diagram of the 34-state LB model.

$$\frac{\partial \rho}{\partial t} + p\, \boldsymbol{\nabla} \cdot (\rho \mathbf{u}) = 0, \tag{16}$$

$$\frac{\partial (\rho \mathbf{u})}{\partial t} + p\, \boldsymbol{\nabla} \cdot \Pi = 0, \tag{17}$$

where Π is the momentum flux tensor

$$\Pi = \sum_{ij} \mathbf{c}_{ij}\mathbf{c}_{ij} \left[f_{ij}^{eq} + \left(1 - \frac{1}{2\tau} \right) f_{ij}^{(1)} \right]. \tag{18}$$

An appropriate choice for local equilibrium distribution function f_{ij}^{eq} can lead to the desired hydrodynamic equations. In order to demonstrate the unique nearest neighbor advection feature, in this paper we adopt the so called 34-state multispeed LB model with three energy levels [11], $j = 0,1,2$. Figure 1 shows the diagram of the model. f_{ij}^{eq}, up to third order, is given as follows:

$$f_{ij}^{eq} = \rho g_j(T) \left[1 + \frac{\mathbf{c}_{ij}\cdot\mathbf{u}}{T} + \frac{(\mathbf{c}_{ij}\cdot\mathbf{u})^2}{2T^2} - \frac{\mathbf{u}^2}{2T} + \frac{(\mathbf{c}_{ij}\cdot\mathbf{u})^3}{6T^3} \right.$$
$$\left. - \frac{\mathbf{c}_{ij}\cdot\mathbf{u}}{2T^2}\mathbf{u}^2 \right], \tag{19}$$

where

$$g_0(T) = 1 - (3T - 3T^2), \tag{20}$$

$$g_1(T) = \frac{2T - 3T^2}{12}, \tag{21}$$

$$g_2(T) = \frac{3T^2 - T}{24}. \tag{22}$$

The temperature value T can vary from $1/3$ to $2/3$ [11,12]. It can be shown that the zeroth and first order momentum flux forms are given as

$$\Pi^{(0)} = \sum_{ij} \mathbf{c}_{ij}\mathbf{c}_{ij} f_{ij}^{eq} = P\mathbf{I} + \rho\mathbf{u}\mathbf{u}, \tag{23}$$

$$\Pi^{(1)} = \left(1 - \frac{1}{2\tau} \right) \sum_{ij} \mathbf{c}_{ij}\mathbf{c}_{ij} f_{ij}^{(1)} = -p\rho\nu \left[2\mathbf{S} - \frac{2}{D}(\boldsymbol{\nabla}\cdot\mathbf{u})\mathbf{I} \right], \tag{24}$$

where $\mathbf{I}$ is the unit second-rank tensor, kinematic viscosity is $\nu = (\tau - \frac{1}{2})T$, and strain tensor is $S_{\alpha\beta} = \frac{1}{2}\left(\frac{\partial u_\alpha}{\partial x_\beta} + \frac{\partial u_\beta}{\partial x_\alpha} \right)$.

Rescaling the time and viscosity by

$$t' = pt, \tag{25}$$

$$\nu' = p\nu = pT(\tau - \tfrac{1}{2}), \tag{26}$$

the resulting rescaled hydrodynamic equations are shown as follows:

$$\frac{\partial \rho}{\partial t'} + \boldsymbol{\nabla} \cdot (\rho \mathbf{u}) = 0, \tag{27}$$

$$\frac{\partial (\rho \mathbf{u})}{\partial t'} + \boldsymbol{\nabla} \cdot (\rho \mathbf{u}\mathbf{u}) = -\boldsymbol{\nabla}P + \boldsymbol{\nabla} \cdot \left[\rho\nu'\left(2\mathbf{S} - \frac{2\mathbf{I}}{D}\boldsymbol{\nabla}\cdot\mathbf{u} \right) \right]. \tag{28}$$

Consequently we have demonstrated that the present volumetric scheme recovers the Navier-Stokes equations at the same order of accuracy as the standard LBM without any additional approximations. Moreover, the scheme immediately illustrates two appealing advantages over the standard LBM. First, the LBM stability is substantially improved with a more relaxed CFL condition. In the present scheme, the

CFL number is reduced from $\Delta t |\mathbf{c}_{ij}| / \Delta x$ to $p \Delta t |\mathbf{c}_{ij}| / \Delta x$, since the fraction factor p is always less than unity. Second, the resulting viscosity ν is reduced by factor p. This helps to achieve lower viscosity (higher Reynolds number) at a given relaxation time τ. On the other hand, the total computational time steps are increased by a factor of $1/p$ compared to the standard LBM in order to simulate the same physically defined time duration. Compared with the previous volumetric schemes [7,8], the present scheme should have a better computational performance for LB models with multiple speed levels, since it has advections only involving nearest neighbor lattice sites.

Because of the fractional factor, particle advection is no longer exact as in the standard LBM: there exists a numerical diffusion at higher than the viscous order. In other words, there is an equivalent hyper-viscosity effect in the volumetric scheme. Nevertheless, unlike the volumetric scheme of Chen [7], the present formulation does not contain numerical diffusion in directions transverse to any microscopic particle velocity. This is due to the fact that the fractional advection is exactly along the particle velocity characteristic line, and no interpolation in any transverse directions is imposed. Since the current scheme has the same overall order of accuracy as the standard LBM, it is expected to capture flow structures as well as that of the standard LBM. The hyperviscous effect should only manifest itself in small flow structures near the grid resolution scale. The numerical investigation of the accuracy and stability of the present volumetric scheme is presented in the next section.

III. NUMERICAL TESTS

A. Poiseuille flow

First, the two-dimensional Poiseuille flow is chosen to investigate the accuracy of the scheme. It is a simple two-dimensional flow in a straight channel driven by a constant pressure gradient force. The analytical solution for such a steady flow is given by

$$\mathbf{u} = \frac{h^2 \mathbf{g}}{2\nu} \frac{y}{h} \left(1 - \frac{y}{h} \right) = 6 \mathbf{u}_{mean} \frac{y}{h} \left(1 - \frac{y}{h} \right), \qquad (29)$$

where h is the width of the channel and $\mathbf{g}$ is the constant pressure gradient force along the streamwise ($\mathbf{x}$) direction.

We performed a series of simulations at various resolutions, $h = 30$, 40, 50, 60, and 70. The well known "half-way" bounce back boundary condition is applied at both the upper and lower channel walls and the periodic boundary condition is imposed in the streamwise direction. In these calculations, the fractional factor p is set to 0.5, and $\mathrm{Re} = (h u_{mean})/\nu$ is 1000. The mean velocity u_{mean} is fixed at a constant value of 0.0667 in lattice units, and the corresponding u_{max} is 0.1. For simplicity, all simulations are carried out isothermally at temperature $T = 0.5$. Figure 2 shows the comparison of the velocity profiles at different resolutions with the analytical solution. All the velocities and distances are normalized by u_{mean} and the width of the channel h, respectively. It is seen that there is a higher order numerical error (hyperviscous effect) in the current scheme and its magnitude decreases
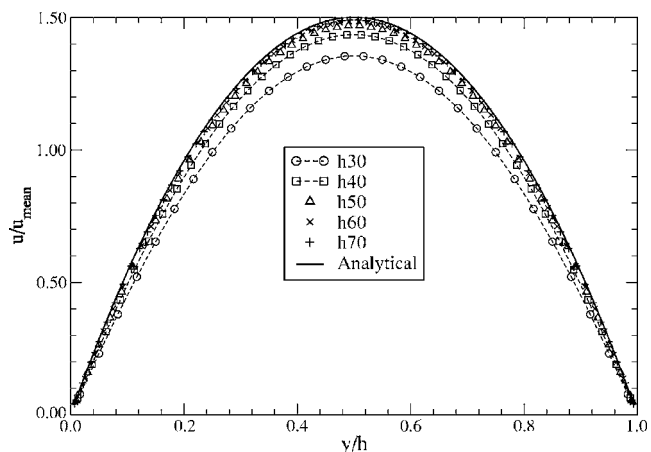

FIG. 2. Steady state velocity profile in the two-dimensional Poiseuille flow at Re = 1000. The solid line is the analytical solution. The symbols represent different resolution all with $p = 0.5$. All quantities are normalized by characteristic values of the flow.

rapidly as resolution increases. The behavior of this numerical error in relation to resolution is shown in Fig. 3. The circles represent the measured deviation of the maximum velocity in these simulations from that of the analytical value. The solid line is a curve fit with a leading term proportional to $(\Delta x)^3$ indicating the numerical diffusion is at least two orders higher than that of the regular physical viscosity. As shown in the figure, the maximum velocity deviation is less than 1% when the resolution is over 60 cells across the width of the channel. Furthermore, we want to address the importance of the first order gradient correction in Eq. (11). Without such a gradient term, the resulting momentum flux term can be theoretically shown to have a resolution dependent regular viscosity (as opposed to a hyperviscosity). This is to be compared with the exact Navier-Stokes form [see Eq. (11)] when the gradient term is included. Figure 4 shows the results of the maximum velocity error from two sets of simulations that are with (circle) and without (square) the gradient term. The Re number here is 10. With-

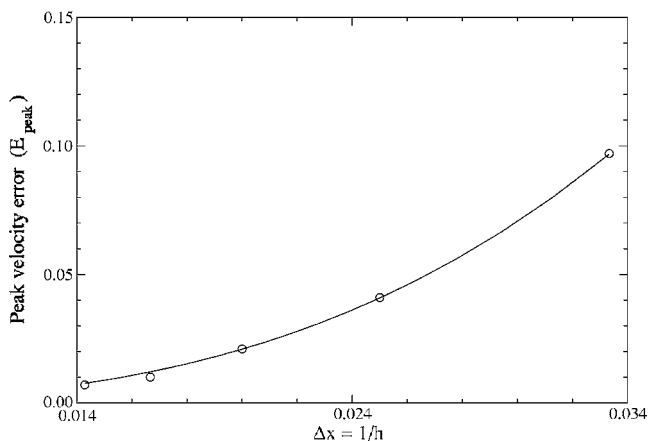FIG. 3. Peak velocity error vs grid size in the two-dimensional Poiseuille flow at Re = 1000 and $p = 0.5$. $E_{peak} = |\max(u_{sim}) - \max(u_{anal})| / \max(u_{anal})$. Circles represent numerical results and solid line represents a fitting curve with decaying rate $\sim (\Delta x)^3$.
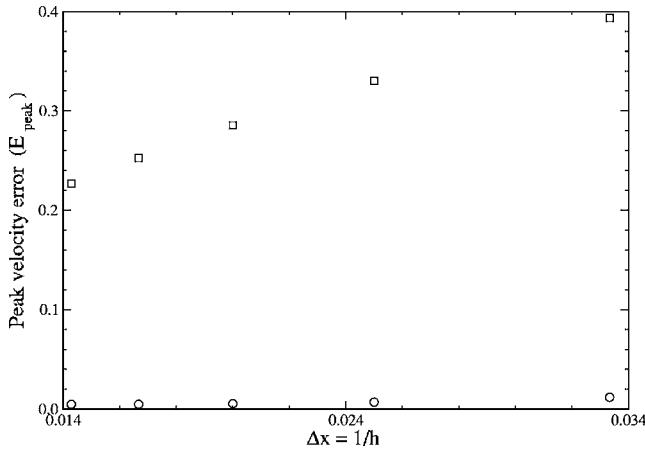
FIG. 4. Peak velocity error vs grid size in the two-dimensional Poiseuille flow at Re=10 and $p=0.5$. $E_{peak}=|\max(u_{sim})-\max(u_{anal})|/\max(u_{anal})$. Circles are results with the first order gradient correction and squares are results without the gradient correction.

FIG. 5. Dimensionless measured and theoretical viscosities vs wavelength (in cell unit) in shear momentum wave decay at Re=128. $1/\mathrm{Re}_{resulted}=\nu_{meas}/(u_0 L)$. The solid line represents the theoretical value of $1/\mathrm{Re}$. The circles, squares and triangles are for $p=1$, 0.5, and 0.25, respectively.

out the gradient term, the error is several orders of magnitude larger than that with the gradient term, and the convergence rate of the former is roughly linear. This error is even greater relative to the true viscosity at higher Re numbers. Hence, the gradient term is essential to ensure a second order accurate LBM scheme in the present formulation.

B. Shear momentum wave decay

To further verify the accuracy of the scheme, a two-dimensional sinusoidal momentum shear wave decay at various wave length is simulated.

The flow is initialized as a transverse sinusoidal wave in that the flow velocity is in the x direction and it varies sinusoidally in the y direction

$$u_x(y,t=0) = 0.1 \sin\left(\frac{2\pi}{L}y\right), \qquad (30)$$

where L is the wavelength. Periodic boundary condition is applied in all directions. It is known that the shear wave decays exponentially in time due to viscosity. Three values of $p=0.25$, 0.5, and 1, are used to investigate if the accuracy has any dependence on p. All simulations are performed with Re=128 and $T=0.5$. Since the valid range of p for the currently used three-speed LB model is $0<p\leq0.5$, the results at $p=1$ are actually calculated using standard LBM. Figure 5 shows the measured viscosities [in a dimensionless form, $1/\mathrm{Re}_{resulted}=\nu_{meas}/(u_0 L)$] at different wavelength values (in terms of lattice units), where $u_0=0.1$ and ν_{meas} is the viscosity value measured from each of these simulations. The circles, squares, and triangles represent simulations with $p=1$, 0.5, and 0.25, respectively. The solid line represents the theoretical viscosity value given by Eq. (26). One can see that the discrepancy between the measured and theoretical values for $p=0.5$ and 0.25 is peaked at short wavelengths and decreases sharply as wavelength increases. As wavelength becomes sufficiently long ($L\geq32$), the error becomes
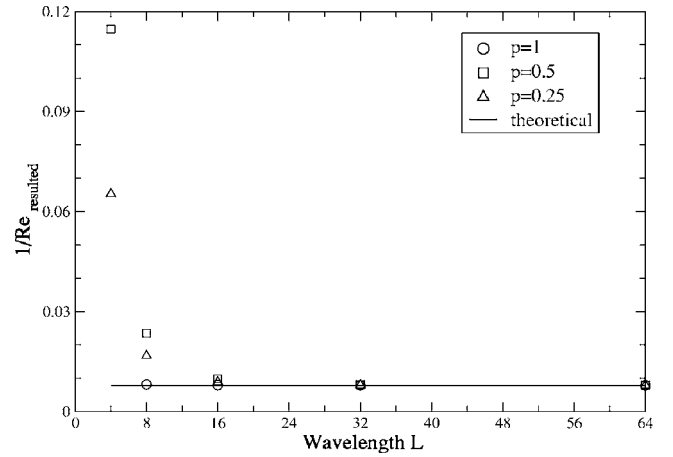
vanishingly small. We wish to emphasize that results for wavelengths with eight lattice points or less correspond to extreme situations, which are impractical for performing simulations at such a Reynolds Number (Re=128). Notice though the standard LBM ($p=1$) shows the similar behavior with a much smaller discrepancy at the short wavelengths, it becomes unstable (oscillating) at $L=4$. Thus it confirms that the present scheme indeed recovers the correct Navier-Stokes behavior as that of the standard LBM at the long wavelength limit, and the numerical error is shown as a higher order numerical effect. This hyperviscouslike effect only damps out small fluid structures close to the spatial resolution scale, and has little impact on large scale flows. Therefore, numerical results are rapidly improved as one applies higher resolutions. A side benefit of such a hyperviscous effect is the improvement of numerical stability, which is confirmed by the simulations at $L=4$ here. Numerical fluctuations at the grid scale are suppressed by such an effect. Figure 5 also indicates that the hyperviscous effect varies with the parameter p. To further investigate the dependence of numerical error on p, we performed simulations on a set of p values for a specific wavelength of $L=16$, shown in Fig. 6. As observed, the numerical error is reduced as p decreases. The reduction of p not only creates a more relaxed CFL condition, but also allows a relatively large relaxation time τ for a given theoretical viscosity. However, the price paid with a smaller p is that more time steps are required to simulate the same physical time.

C. Two-dimensional lid-driven cavity flow

As the third and final test, we choose the benchmark case of two-dimensional cavity flow to demonstrate the overall quality of our present scheme. This case has been well studied due to its simple geometry and complex nonlinear flow structures. Our simulation results are directly compared with the direct numerical simulation (DNS) results of Ghia *et al.* [13] and the LBM results of Hou [14].
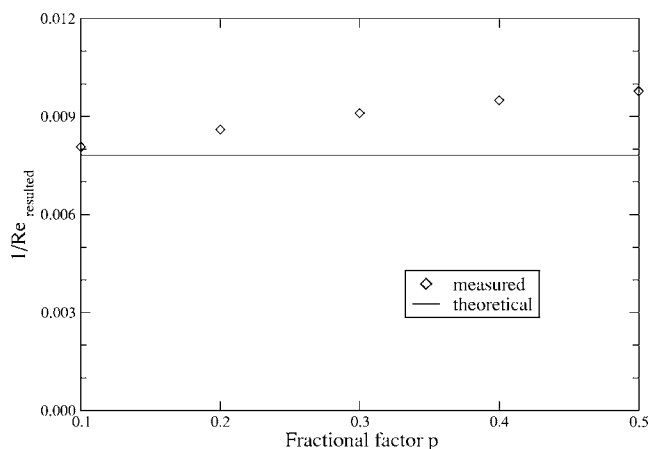
FIG. 6. Dimensionless measured and theoretical viscosities vs fractional factor p in shear momentum wave decay at Re=128 and L=16 (in cell unit). $1/\mathrm{Re}_{resulted} = \nu_{meas}/(u_0 L)$. The solid line represents the theoretical value of $1/\mathrm{Re}$. The diamonds are for measured values.

The test is defined by a 100×100 lattice square domain with the half-way bounceback boundary condition everywhere except for the top lid moving with a uniform velocity of U=0.1. Simulations are conducted for a wide range of Reynolds numbers from 100 to 7500, with p=0.5 and T=0.5 as in the previous tests. The flow structures in all our simulations agree well with the known published results [13,14]. In addition to the large primary vortex in the center, two small secondary counter-rotating vortexes appear in the bottom corners of the cavity. The locations and sizes of these vortexes strongly depend on the values of Reynolds number. As Re reaches to 2000, a third vortex is developed in the upper left corner (Fig. 7). As Re further increases, the corner vortexes become stronger and more and more small flow structures emerge.

Direct comparison of the locations of the vortex centers are listed in Table I. Our simulation results show good quan-
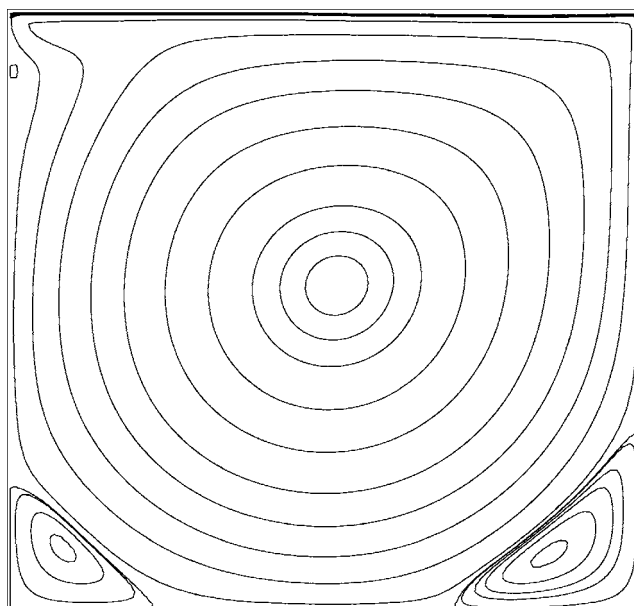

FIG. 7. Stream line of Re=2000 and p=0.5 in the cavity. Resolution is 100×100. The lid is moving from left to right. Re $= UL/\nu$, where U is the velocity of the lid and L is the size of the cavity.

titative agreements with other bench mark results [13,14]. Besides the primary vortex, all three corner vortexes are well reproduced. It is worth noting here that Hou's resolution is 256×256 and ours is 100×100. This is mainly because of the well known stability limitation of the former: the standard LBM becomes numerically unstable for Re greater than 2000 at resolution 100^2. On the contrary, our scheme is stable for Re up to 7500 or higher at this resolution. The hyperviscous numerical effect greatly improves numerical stability while the scheme still captures accurately most of the flow structures. Figure 8 shows streamlines of one of our simulations with Re=7500. Indeed, except the size of the left

TABLE I. Vortex locations in a two-dimensional (2D) cavity. a: Ghia *et al.* (see Ref. [13]); b: Hou (see Ref. [14]); c: present work. All locations normalized by the size of cavity.

| Re		Primary vortex	Lower left	Lower right	Upper left
100	a	(0.6172, 0.7344)	(0.0313, 0.0391)	(0.9453, 0.0625)	
	b	(0.6196, 0.7373)	(0.0392, 0.0353)	(0.9451, 0.0627)	
	c	(0.6139, 0.7288)	(0.0372, 0.0373)	(0.9423, 0.0598)	
1000	a	(0.5313, 0.5625)	(0.0859, 0.0781)	(0.8594, 0.1094)	
	b	(0.5333, 0.5647)	(0.0902, 0.0784)	(0.8667, 0.1137)	
	c	(0.5304, 0.5584)	(0.0823, 0.0739)	(0.8670, 0.1062)	
2000	b	(0.5255, 0.5490)	(0.0902, 0.1059)	(0.8471, 0.0980)	
	c	(0.5171, 0.5414)	(0.0877, 0.1074)	(0.8484, 0.0937)	
5000	a	(0.5117, 0.5352)	(0.0703, 0.1367)	(0.8086, 0.0742)	(0.0625, 0.9102)
	b	(0.5176, 0.5373)	(0.0784, 0.1373)	(0.8078, 0.0745)	(0.0667, 0.9059)
	c	(0.5099, 0.5280)	(0.0833, 0.1243)	(0.8228, 0.0858)	(0.0477, 0.9038)
7500	a	(0.5117, 0.5322)	(0.0645, 0.1504)	(0.7813, 0.0625)	(0.0664, 0.9141)
	b	(0.5176, 0.5333)	(0.0706, 0.1529)	(0.7922, 0.0667)	(0.0706, 0.9098)
	c	(0.5083, 0.5278)	(0.0781, 0.1425)	(0.8005, 0.0760)	(0.0551, 0.8962)
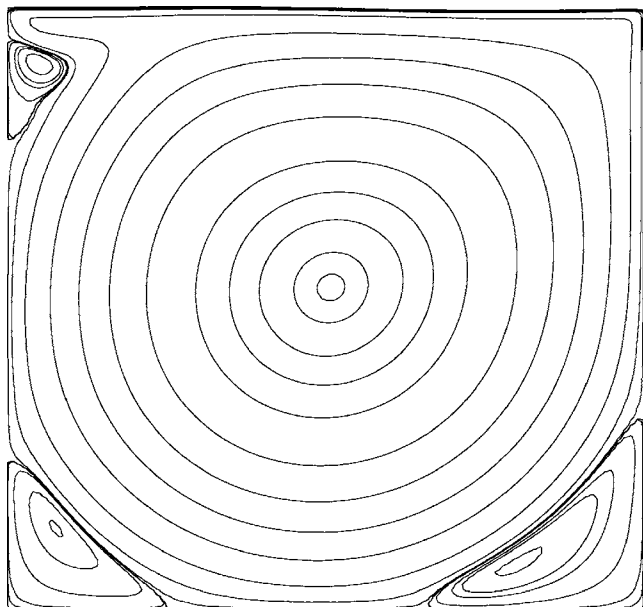
FIG. 8. Stream line of Re=7500 and p=0.5 in the cavity. Resolution is 100×100. The lid is moving from left to right. Re $=UL/\nu$, where U is the velocity of the lid and L is the size of the cavity.

upper vortex is slightly smaller than Hou's high resolution based results, all other flow features are very well predicted.

IV. CONCLUSION AND DISCUSSION

In this paper, we have presented an extended fractional volumetric LB scheme. This scheme is particularly desirable for LB models involving multiple speed levels. It achieves a local advection process that only includes nearest neighbor lattice cells, even for particles with speed higher than one lattice unit. This local one-cell advection is especially advantageous in that it can efficiently reduce the amount of data communication and, hence, improve the parallel computation efficiency and scalability.

We have also shown that the present scheme recovers the Navier-Stokes equations at the same order of accuracy as the standard LBM without any additional approximations. In addition, the present scheme has demonstrated a better stability than the standard LBM due to the improved CFL condition. By effectively reducing viscosity by the fractional advection factor p, this scheme is shown to be significantly more robust at high Reynolds numbers in which the standard LBM fails. On the other hand, a hyperviscous numerical effect exists in the present scheme. Such a high order numerical diffusion effect decreases rapidly either as the overall resolution is increased or the flow scale of interest is much larger than that of the lattice grid spacing. Since it is only effective at near grid scale wavelengths, the hyperviscosity also helps to further enhance the numerical stability over the standard LBM, as shown in the cavity simulations above.

The numerical algorithm of the present volumetric scheme is rather simple structurally and very easy to implement. Regarding the computational cost, the current scheme increases the total simulation time steps by a factor of $1/p$ in order to achieve the same physical time as the standard LBM. However, with a much-enhanced stability, the scheme can achieve high Reynolds number at lower resolutions. This in turn reduces the overall computational cost. Together with the advantage of achieving local advection for all particle speed levels, the overall computational cost associated with the current scheme is promising. Finally, we want to point out that this scheme is particularly good for LB models involving noninteger particle speeds [15].

[1] R. Benzi, S. Succi, and M. Vergassola, Phys. Rep. **222**, 145 (1992).

[2] H. Chen, S. Chen, and W. Matthaeus, Phys. Rev. A **45**, R5339 (1992).

[3] S. Chen and G. D. Doolen, Annu. Rev. Fluid Mech. **30**, 329 (1998).

[4] H. Chen, S. Kandasamy, S. Orszag, R. Shock, S. Succi, and V. Yakhot, Science **301**, 633 (2003).

[5] N. Cao, S. Chen, S. Jin, and D. Martinez, Phys. Rev. E **55**, R21 (1997).

[6] J. D. Sterling and S. Chen, J. Comput. Phys. **123**, 196 (1996).

[7] H. Chen, Phys. Rev. E **58**, 3955 (1998).

[8] R. Zhang, H. Chen, Y. Qian, and S. Chen, Phys. Rev. E **63**, 056705 (2001).

[9] S. Chen, H. Chen, D. Martinez, and W. Matthaeus, Phys. Rev. Lett. **67**, 3776 (1991).

[10] U. Frisch, D. D'Humieres, B. Hasslacher, P. Lallemand, Y. Pomeau, and J. Rivet, Complex Syst. **1**, 649 (1987).

[11] H. Chen, C. Teixeira, and K. Molvig, Int. J. Mod. Phys. C **8**, 675 (1997).

[12] H. Chen and C. Teixeira, Comput. Phys. Commun. **129**, 21 (2000).

[13] U. Ghia, K. N. Ghia, and C. Y. Shia, J. Comput. Phys. **48**, 387 (1982).

[14] S. Hou, Ph.D. thesis, Kansas State University, Kansas, 1995.

[15] X. Shan, X. Yuan, and H. Chen, J. Fluid Mech. **550**, 413 (2006).